Correlation between crystal purity and the charge density wave in 1*T*-VSe_2

C. J. Sayers,[1,*] L. S. Farrar,[1] S. J. Bending,[1] M. Cattelan,[2] A. J. H. Jones,[3] N. A. Fox,[2,3] G. Kociok-Köhn,[4] K. Koshmak,[5] J. Laverock,[3] L. Pasquali,[5,6,7] and E. Da Como[1]

[1]*Centre for Nanoscience and Nanotechnology, Department of Physics, University of Bath, Bath BA2 7AY, United Kingdom*
[2]*School of Chemistry, University of Bristol, Cantocks Close, Bristol BS8 1TS, United Kingdom*
[3]*HH Wills Physics Laboratory, University of Bristol, Tyndall Avenue, Bristol BS8 1TL, United Kingdom*
[4]*Material and Chemical Characterisation Facility (MC²), University of Bath, Claverton Down, Bath BA2 7AY, United Kingdom*
[5]*IOM-CNR Institute, Area Science Park, SS 14 Km, 163.5 Basovizza, 34149 Trieste, Italy*
[6]*Dipartimento di Ingegneria "Enzo Ferrari," Università di Modena e Reggio Emilia, via P. Vivarelli 10, 41125 Modena, Italy*
[7]*Department of Physics, University of Johannesburg, P.O. Box 524, Auckland Park 2006, South Africa*

(Received 13 August 2019; accepted 21 January 2020; published 11 February 2020)

We examine the charge density wave (CDW) properties of 1*T*-VSe_2 crystals grown by chemical vapor transport (CVT) under varying conditions. Specifically, we find that upon lowering the growth temperature ($T_g < 630\,^{\circ}$C), there is a significant increase in both the CDW transition temperature and the residual resistance ratio (RRR) obtained from electrical transport measurements. Using x-ray photoelectron spectroscopy, we correlate the observed CDW properties with stoichiometry and the nature of defects. In addition, we have optimized a method to grow ultrahigh-purity 1*T*-VSe_2 crystals with a CDW transition temperature $T_{CDW} = (112.7 \pm 0.8)$ K and maximum residual resistance ratio RRR ≈ 49, which is the highest reported thus far. This work highlights the sensitivity of the CDW in 1*T*-VSe_2 to defects and overall stoichiometry and the importance of controlling the crystal growth conditions of strongly correlated transition metal dichalcogenides.

DOI: 10.1103/PhysRevMaterials.4.025002

I. INTRODUCTION

The metallic transition metal dichalcogenides (TMDs) are well known to exhibit interesting strongly correlated behavior such as charge density waves (CDWs) [1,2] and superconductivity. In 1*T*-VSe_2, an incommensurate CDW develops at $T_{CDW} = 110$ K with $4a \times 4a \times 3.18c$ periodic lattice distortion, followed by a further change in the distorted *c*-axis to $3.25c$ below 85 K [3]. Signatures of these phase transitions have been noted in x-ray [3] and electron diffraction [4], magnetic, and transport studies [5]. The CDW is likely driven by Fermi surface nesting involving states along the flat portions of the electron pocket centered around the $\overline{M}$ point at the edge of the Brillouin zone [6], which possibly has a three-dimensional character [7]. The common polytype of VSe_2 has the trigonal (1*T*) unit cell and belongs to the $P\bar{3}m1$ space group [4]. Figures 1(a) and 1(b) show the layered structure consisting of Se-V-Se planes in the *a*-*b* direction separated by a van der Waals (vdW) gap and octahedral metal coordination when viewed along the *c*-axis.

In addition to the ongoing efforts to understand CDW transitions in bulk TMDs, the recent surge in research on layered 2D materials has reignited interest in this area. So far, it has been shown that 1*T*-VSe_2 has a large range of tunability of its CDW properties with dimensionality, as the transition temperature and magnitude of the order parameter are strongly influenced by the sample thickness on a nanometer scale [8,9]. Control of the distorted lattice periodicity is also possible by strain engineering, and an unconventional $(4a \times \sqrt{3}a)$ CDW has been observed by STM [19]. At the monolayer limit, there have been reports of possible ferromagnetism [10–12], strongly enhanced CDW order evidenced by a fully gapped Fermi surface [13], and an increase in the transition temperature up to $T_{CDW} = 220$ K [14].

With increasing interest in studying monolayer or few-layer charge density wave TMDs, the bottom-up approach of growth by molecular beam epitaxy [13,19] or chemical vapor deposition (CVD) [15,16] techniques has become common. Once optimized, these methods are excellent at producing thin films. However, samples produced this way often suffer from a high number of crystal defects. In particular, the presence of grain boundaries due to coalescing nucleation sites is a common and well-documented problem in 2D materials grown by CVD, such as graphene [17]. Also, there is often an unavoidable interaction with the growth substrate such as doping [18] or strain [19] which can alter the sample properties. Instead, a top-down approach by exfoliation of high-quality crystals as the starting material is still considered the ideal way to obtain pristine monolayers and to provide the basis for construction of vdW heterostructures by dry transfer [20].

At present, many researchers either grow their own crystals or obtain them commercially. In both cases, the specific growth conditions are often not reported. However, notably among the TMDs, 1*T*-VSe_2 can grow far from ideal stoichiometry under varying conditions [21]. Previous investigations on 1*T*-VSe_2 have suggested that the CDW transition temperature is maximum for samples prepared using the lowest growth temperatures ($T_g < 600\,^{\circ}$C), where the Se:V

*Corresponding author: c.j.sayers@bath.ac.uk

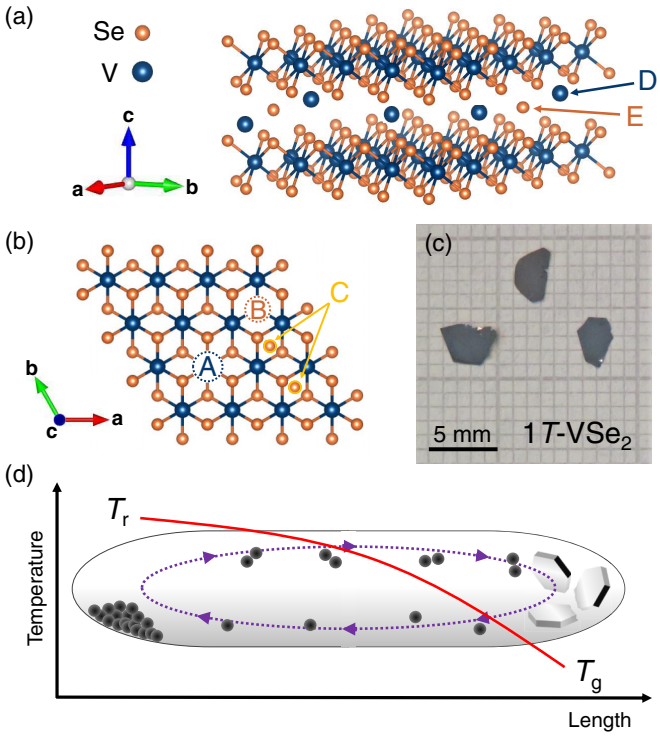

FIG. 1. Growth of 1*T*-VSe_2 crystals. (a), (b) Crystal structure of 1*T*-VSe_2 viewed along the layer plane and *c*-axis, respectively. Common defect types found in TMDs are labeled. In 1*T*-VSe_2, these correspond to vanadium and selenium vacancies (A and B), selenium aggregates/clusters (C), and interstitials in the van der Waals gap between the layer planes (D and E). (c) Image of typical crystals produced by chemical vapor transport (CVT). (d) Illustration of the CVT process. Iodine vapor carries material from the reaction zone at T_r to the growth zone at T_g, where crystals form. The solid red line is a sketch of a typical temperature profile.

ratio is expected to approach 2:1 [22,23]. Deviations from ideal stoichiometry due to increasing density of defects can occur at higher growth temperatures, but their nature in this compound remains unknown. Types of defects that are typically found in TMD crystals are labeled in Figs. 1(a) and 1(b) including vacancies and interstitials [24]. The influence of growth temperature on crystal purity and its relation to CDW properties has been reported in the related compound 1*T*-$TiSe_2$. Increasing Ti interstitials in the vdW gap between the layers results in electron doping and reduces T_{CDW} by upsetting the delicate balance of electrons to holes, which has consequences within the excitonic insulator scenario [25]. In 1*T*-VSe_2, where Fermi surface nesting is suggested to play a role, such a doping effect could have a significant impact on the CDW by altering the topology of the Fermi surface due to the change in chemical potential. Thus far, a detailed study of the growth conditions of 1*T*-VSe_2 in relation to its CDW properties and the role of defects is lacking.

Here, we show that changes in the growth temperature over the range 550 °C–700 °C have a significant impact on the physical purity, structure, and intrinsic stoichiometry which subsequently influences the CDW behavior. Electronic transport measurements show that the CDW transition temperature increases markedly for crystals grown at $T_g < 630$ °C. Using x-ray spectroscopy, we are able to identify defects in samples grown at higher temperatures and correlate this with the observed electronic properties. In addition, we have optimized the conditions for growing ultrapure 1*T*-VSe_2 at $T_g = 550$ °C with a transition temperature $T_{CDW} = (112.7 \pm 0.8)$ K and a maximum residual resistance ratio RRR ≈ 49, which, to the best of our knowledge, surpasses the highest value ($\sim$28) reported previously, [26,27].

II. EXPERIMENTAL METHODS

A. Crystal growth

1*T*-VSe_2 crystals were grown using a chemical vapor transport (CVT) method [28], whereby a constant temperature gradient drives the crystallization of the elements from a vapor at high temperature as illustrated in Fig. 1(d). High-purity vanadium (99.9%) and selenium (99.99%) powders were sealed inside an evacuated quartz ampoule, together with anhydrous iodine (99.998%), which acts as the transport agent. Under an inert atmosphere (N_2 glovebox), stoichiometric amounts of the elements (2:1 molar ratio) were loaded, plus a slight excess of selenium (2.4–3.4 mg cm^{-3}), based on the ampoule volume. The amount of iodine (2.10–2.25 mg cm^{-3}) was chosen to facilitate growth within a reasonable time frame [29], while also minimizing the potential for iodine to be introduced into the crystals, which is known to suppress the CDW transition in other TMDs [25]. The ampoule was evacuated using a pump capable of achieving a base pressure of 7×10^{-6} mbar and then sealed with a flame. A two-zone tube furnace was used with a temperature gradient between hot (reaction temperature; T_r) and cold (growth temperature; T_g) zones of $\Delta T = (55\,°\text{C}–60\,°\text{C})$, which was confirmed with a thermocouple probe. The temperature stability was better than ± 1 °C. Growth proceeded for up to 21 days, resulting in many crystals of ($5 \times 5 \times 0.1$ mm) forming at the cold end of the ampoule. The crystals were typically thin platelets with hexagonal edges and a highly reflective silver appearance as shown in Fig. 1(c).

Under these general conditions, this procedure was carried out several times in order to produce separate sample batches with different growth temperatures T_g in the range 550 °C–700 °C.

B. Electronic transport

We measured the resistance as a function of temperature, $R(T)$, for different crystal batches. Samples were cut with a razor blade into rectangular shapes (typical lateral size, 4×1 mm) and mounted on electrically insulating substrates using thermal varnish. Contacts were made to the as-grown crystal surfaces using silver paste in a standard four-point configuration. Measurements were performed in a JANIS 4 K closed-cycle cryocooler (4–300 K) using a lock-in amplifier (SR830) and a typical excitation current of 1 mA.

Multiple crystals were measured from each batch to investigate any possible variations.

C. X-ray spectroscopy

We used both x-ray photoelectron spectroscopy (XPS) and x-ray absorption spectroscopy with synchrotron radiation to study core levels of selenium (Se), vanadium (V), and iodine (I) in 1T-VSe_2. Measurements were performed at the BEAR end station (Elettra synchrotron, Trieste) [30,31]. In order to expose a clean surface, the samples were cleaved in a nitrogen glove-bag attached to the fast entry of the preparation chamber.

We found that after prolonged exposure, we were able to induce radiation damage to the sample surface, which resulted in noticeable changes in the spectra. Hence, for the results presented here and in the Supplemental Material [32], we minimized both the exposure time and the photon flux (e.g., $\sim 7 \times 10^{10}$ photons s^{-1} at $h\nu = 150$ eV). Identical experimental conditions were maintained for each sample. As a result of these measures, we did not observe any evolution of the spectra during the measurements which could be related to damage, and therefore the properties we report are intrinsic to the samples.

III. ELECTRONIC PROPERTIES

To investigate the bulk electronic properties of 1T-VSe_2, we measured the resistance as a function of temperature, $R(T)$, for different crystal batches as shown in Fig. 2(a). The shape of the curve agrees with previous studies on 1T-VSe_2 and shows an overall metallic behavior with a slight increase in the resistance related to the CDW transition at $T_{CDW} \approx$ (100–110) K [5,33,34]. At low temperatures, the resistivity approaches a finite value related to the amount of impurity scattering [33]. We do not see any indication of an upturn in the resistance of our samples at a low temperature (4 K), in contrast to a previous study which attributed this behavior to a Kondo effect [35].

The first derivative, dR/dT, in Fig. 2(b) highlights the CDW transition, T_{CDW}, which we define as the onset temperature at which the resistance first starts to increase and corresponds to the point at which dR/dT initially crosses 0 [dashed horizontal line in Fig. 2(b)]. Details of obtaining T_{CDW} in this way are provided in Ref. [32], and we emphasize that using alternative points in dR/dT to define T_{CDW} does not change the observed trend between samples or the conclusions of this work. Figure 3(a) shows the CDW transition temperatures extracted from dR/dT for different sample batches as a function of the growth temperature. The overall trend shows that T_{CDW} is increased at lower growth temperatures, reaching a maximum of $T_{CDW} = (112.7 \pm 0.8)$ K for the 550 °C sample. We note that samples with $T_g < 630$ °C show an increase in transition temperature above the typically reported value of $T_{CDW} = 110$ K. Based on the trend of our samples produced at the lowest growth temperatures, it seems as though T_{CDW} is approaching the inherent maximum for 1T-VSe_2. It is also apparent in Fig. 2(b) that there is an evolution in the width of the dR/dT feature relating to the CDW transition, where there is a broadening at higher growth temperatures. This is seen in both the onset of the transition (gradient of the steep decline near T_{CDW}) and the width of the minima in dR/dT. Such a broadening is often linked to disorder, and the behavior in our

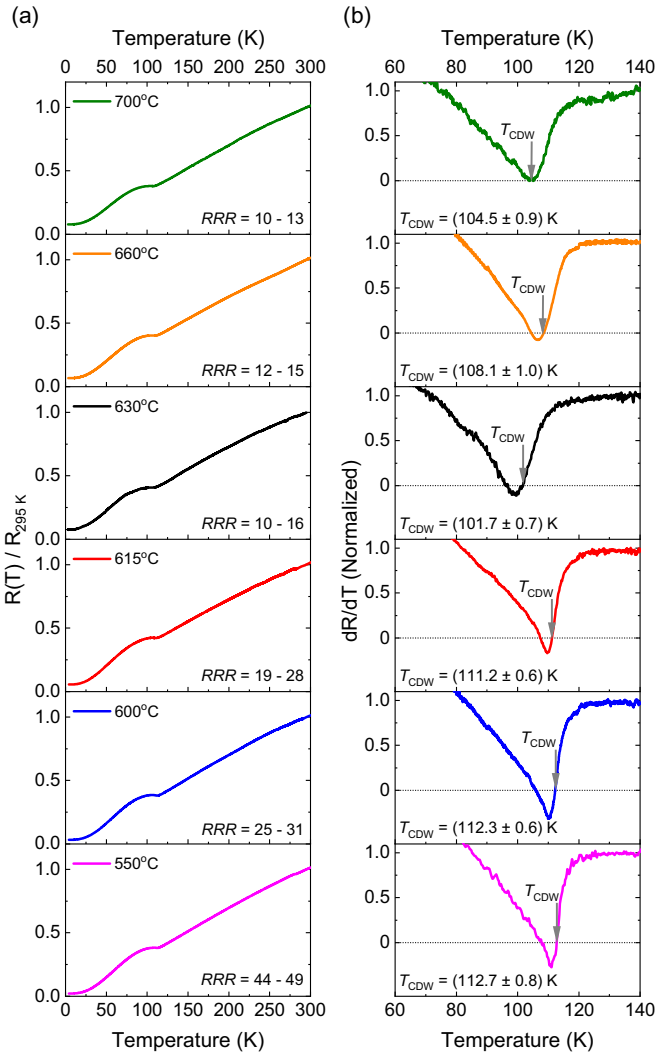

FIG. 2. Resistance of 1T-VSe_2 samples produced at different growth temperatures as indicated. (a) Normalized resistance $R/R_{295\,K}$ for different sample batches. The range of residual resistance ratios (RRRs) for each crystal batch is labeled. (b) First derivative of the resistance, dR/dT, highlighting the charge density wave transition, T_{CDW}, which we define as the point at which dR/dT initially crosses 0, indicated by the arrows.

samples is similar to that observed in $NbSe_2$ using electron irradiation dosing to induce atomic defects without doping the system [37]. Additional information can be extracted from the magnitude of the dR/dT minima below 0 (dashed horizontal line), which also follows a similar trend, as the dR/dT of the sample with the highest T_{CDW} becomes the most negative following the CDW transition. We show in Ref. [32] that this corresponds to the magnitude of the resistance increase at T_{CDW} relative to the normal metallic behavior. Therefore our results are fully consistent with strengthened CDW order where one would expect a more effective gapping of the Fermi surface, as the proportion of charge carriers removed at T_{CDW} is greater.

The residual resistance ratio is a well-known parameter often used to estimate the purity of metals. At sufficiently low temperatures, the scattering of carriers is dominated by

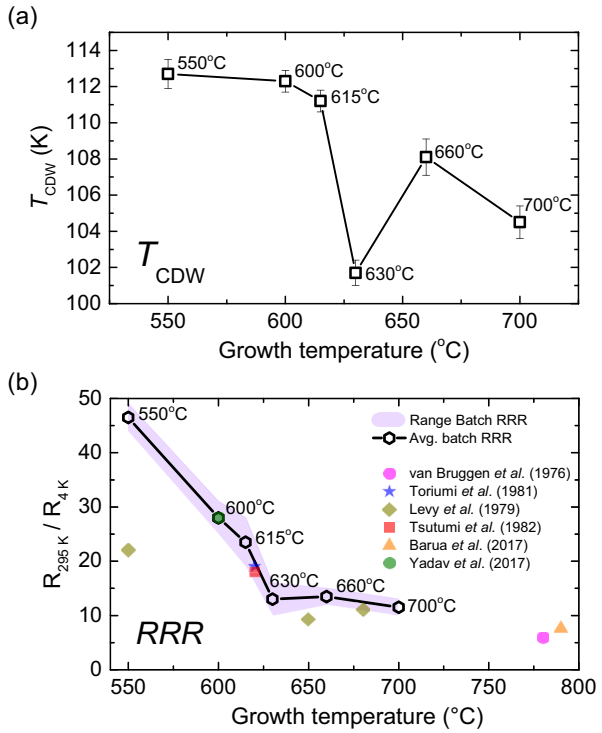

FIG. 3. Electronic properties of 1*T*-VSe_2 samples as a function of the crystal growth temperature, T_g. (a) charge density wave transition temperature, T_{CDW}. (b) Average residual resistance ratio (RRR), $R_{295\,K}/R_{4\,K}$. The shaded area corresponds to the RRR range found within each batch of crystals. For comparison, the colored data points show RRR values taken from the literature as indicated. If the value was not directly quoted in those works, it has been estimated here from the published resistance/resistivity data.

impurities or crystal defects, which gives rise to a finite (residual) resistance. The magnitude of this residual resistance is thus linked to the density of impurities and/or defects present in the sample. Using the ratio $R_{295\,K}/R_{4\,K}$, we are able to compare several samples as shown in Fig. 3(b). Overall, we find that the average RRR within each batch increases at lower growth temperatures, indicating a reduction in impurity/defect scattering. For samples grown at the lowest temperature (550 °C), we find a maximum RRR of ∼49 within the batch. Similar to the behavior of the CDW transition temperature, there is also a significant increase in the average RRR, from ∼12 to > 22, for samples with $T_g < 630$ °C. This is consistent with the width of the CDW transitions in dR/dT [Fig. 2(b)] for samples with $T_g = 630$ °C–700 °C, confirming a defect-induced broadening. By comparing our results to reports of RRR values in the literature on 1*T*-VSe_2 over a range of growth temperatures, there is a clear agreement with this trend [Fig. 3(b)].

Finally, we discuss the scattering mechanism of charge carriers at low temperatures by analyzing the temperature dependence of the resistance. Previously in 1*T*-VSe_2, there have been reports of a strong T^2 dependence [5,34], which could suggest significant electron-electron scattering. By fitting the low-temperature data in the range (5–15) K with a power law, $R \propto T^x$, we also find a T^2 dependence, but only for the sample grown at the highest temperature (700 °C). By contrast, the sample grown at the lowest temperature (550 °C) shows a T^3 behavior, and there appears to be a progressive shift between these two regimes for intermediate temperatures (see Ref. [32]). In other CDW-bearing TMDs, a temperature dependence in the range T^3–T^5 is found for $T \leqslant$ 25 K, depending on the compound, and is related to electron-phonon scattering [36]. The power then depends on the orbital character of bands involved in either *intraband* or *interband* scattering, the density of states, and the strength of the CDW order (proportion of carriers lost from the Fermi surface). For example, a T^3 dependence is found for the ideal resistivity in 2*H*-$NbSe_2$ and can be understood by a simple two-band model which describes an electron-phonon-mediated interband scattering of *s*-like electrons into the *d* band. Such a two-band analysis has also been used to successfully describe the temperature dependence of the Hall coefficient in 1*T*-VSe_2 [27] and the ideal resistivity was found to be in the range T^3–T^4 for the highest-purity samples.

We therefore suggest that a similar electron-phonon scattering mechanism is the case for pure 1*T*-VSe_2, which is seen here in our sample with the highest RRR (550 °C). Instead, the low-temperature resistance deviates rapidly from this behavior with increasing disorder and approaches a T^2 dependence. Clearly, this behavior seems to be rather sample dependent and could explain the large variation reported in the literature [5,26,27,34].

In summary, the electronic properties of 1*T*-VSe_2 and its CDW behavior vary quite significantly with the crystal growth temperature. The observed trends of T_{CDW} and RRR in Fig. 3 are similar, and therefore the underlying mechanism influencing both of these properties is likely to be intrinsically linked. However, at low growth temperatures (550 °C–600 °C), it appears that the strength of the CDW order (T_{CDW}) approaches its maximum, whereas the crystal purity (RRR) continues to increase.

IV. X-RAY SPECTROSCOPY AND DISCUSSION

To obtain information on the chemical composition of our samples, we used XPS to study core levels in 1*T*-VSe_2. Herein, we mainly discuss the XPS results of the Se-3*d* core levels for which we find a significant variation between our samples. Instead, the vanadium core levels show no noticeable variation and either iodine was not present in our samples or its concentration was below the detectable limit. These results are included in the Supplemental Material [32]. We did not observe any sign of oxidation in the Se-3*d* spectra, which otherwise would be in the form of SeO_2 present at ∼59.9 eV [38] [indicated by the arrow in Fig. 4(d)]. Additionally, the x-ray absorption spectroscopy results near the O *K*-edge showed a negligible amount of oxygen and all samples had identical spectra (see Ref. [32]). Therefore, we rule out the presence of oxygen or iodine as an explanation for the observed change in CDW properties.

XPS spectra for the Se-3*d* core levels of different samples are shown in Fig. 4(a). The main feature is the doublet (labeled) with Se-$3d_{5/2} \approx 53.4$ eV and spin-orbit splitting $\Delta_{so} \approx 0.86$ eV, which corresponds to the Se^{2-} oxidation state of Se bound to V in 1*T*-VSe_2 [12]. An additional feature on the high-energy side was also found in the region of 55–56 eV,

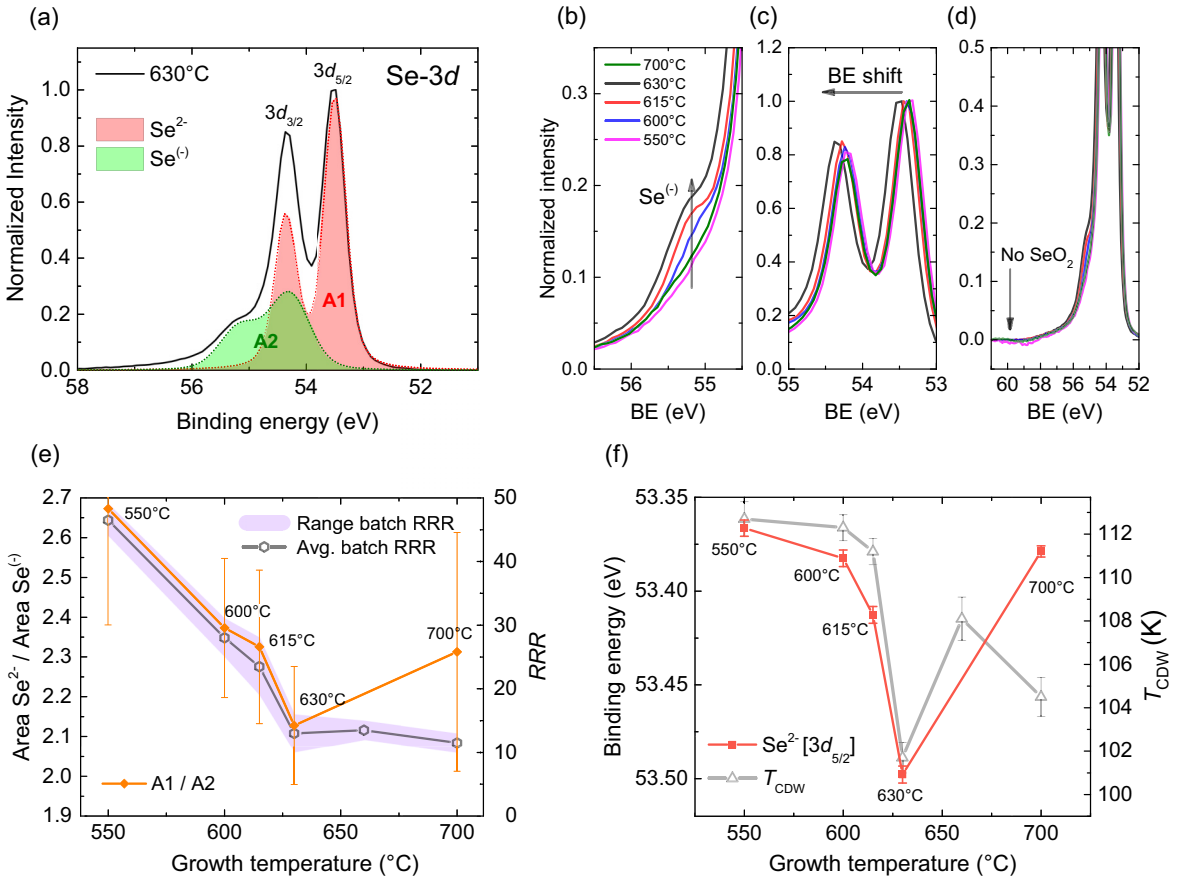

FIG. 4. X-ray photoelectron spectroscopy of 1T-VSe_2 samples grown at different temperatures. (a) Se-3d spectra ($h\nu = 150$ eV). Shaded curves are fits to the data for the $T_g = 630\,^{\circ}$C sample, showing the contribution from Se^{2-} and $Se^{(-)}$ oxidation states. (b)–(d) The same data as in (a), highlighting the feature in Se-3d spectra related to the presence of $Se^{(-)}$, the observed shift in binding energy (BE), and the absence of SeO_2. (e) Area ratio (A1/A2) as a function of the growth temperature, T_g (left axis), obtained from fitting the Se-3d spectra for the Se^{2-} (A1) and $Se^{(-)}$ (A2) oxidation states. A comparison (right axes) is made with the residual resistance ratio (RRR) from electronic transport measurements. (f) BE of the $3d_{5/2}$ peak for Se^{2-} obtained from fitting the data. Error bars in (e) and (f) show the standard deviations on the fitting parameters.

which is highlighted in Fig. 4(b) and shows a clear variation between samples. We find a good fit to the data using two doublets as illustrated in Fig. 4(a) for the $T_g = 630\,^{\circ}$C sample. The binding energy (BE) of the second doublet relating to the additional feature is Se-3$d_{5/2} \approx 54.2$ eV, which we assign to the presence of more positive oxidation states of selenium. Since it appears in our data as a single broad doublet (Gaussian width ∼2 larger than that of Se^{2-}), it is likely to arise from a combination of oxidation states. We label this feature $Se^{(-)}$ since its BE is slightly lower (i.e., more negative) than that of pure selenium, Se^0, which is expected at ∼55.5 eV [38]. Such a feature could indicate the presence of partially bound or unbound Se in the form of vanadium vacancies, in-plane Se aggregates/clusters [12,39], or Se interstitials [18] (see Fig. 1). From the fitting, the contributions of Se^{2-} and $Se^{(-)}$ states in each sample are represented by the shaded areas, A1 and A2, respectively, in Fig. 4(a). The ratio A1/A2 gives an indication of the relative amount of $Se^{(-)}$ oxidation states present in our samples and is shown in Fig. 4(e) as a function of the growth temperature. Comparing this ratio with the RRR from electronic measurements [right axis; Fig. 4(e)], there appears to be a correlation with the overall trend, which suggests that the presence of these $Se^{(-)}$ states contributes to the impurity/defect scattering in electronic transport.

It can also be seen in Fig. 4(c) that there is a shift in binding energy of the Se-3d spectra between samples. We find that this shift is significant (∼120-meV variation), and there is an overall trend of increasing Se^{2-} binding energy for samples grown at higher temperatures as shown in Fig. 4(f). We rule out any energy shift due to local charge effects from an increasing concentration of the more positive $Se^{(-)}$ oxidation states discussed previously, since there is negligible broadening of the observed Se^{2-} linewidth between samples. Such a local effect would rather be expected to contribute multiple environments, leading to the inhomogeneous broadening of the observed core level in addition to a binding energy shift. Instead, the rigid shift of the entire Se-3d states is better explained by a doping effect in our samples. Specifically, an overall electron doping raises the Fermi level, resulting in an apparent shift of core levels to higher binding energies with respect to our XPS energy analyzer. Therefore, we suggest that samples grown at higher temperatures are either V rich ($V_{1+x}Se_2$) or Se deficient (VSe_{2-x}). The BE shift agrees with the evolution of T_{CDW} [right axis in Fig. 4(f)], and hence we

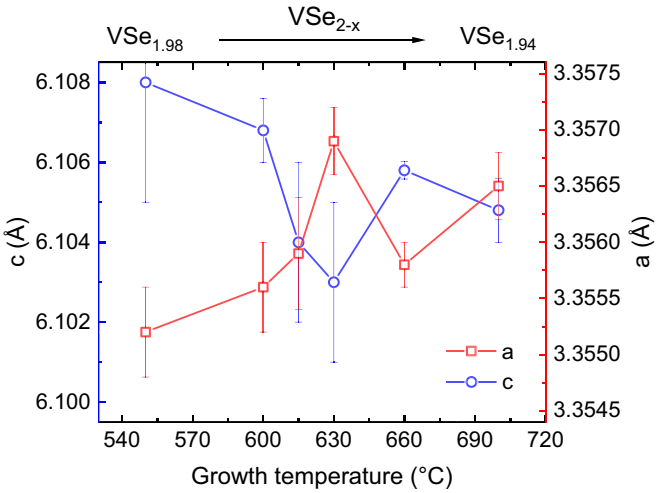

FIG. 5. Lattice parameters of 1*T*-VSe_2 samples obtained from powder x-ray diffraction. The left- and right-axis labels show the *c*- and *a*-axis parameters of the $P\bar{3}m1$ unit cell, respectively. The top-axis labels show a comparison with the overall variation of the crystal stoichiometry (Se/V ratio) obtained from laboratory XPS measurements.

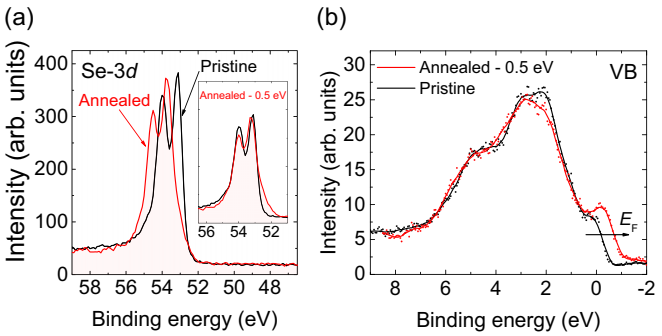

FIG. 6. Effect of annealing on core levels measured by μXPS ($h\nu = 1486.7$ eV). (a) Se-3*d* spectra for the $T_g = 630$°C sample. A comparison is made between the pristine sample (black line) after cleaving in ultrahigh vacuum and the sample after annealing at 520°C for ∼40 min (red line). Inset: The same comparison with a shift of −0.5 eV applied to the annealed sample spectrum. (b) Valence band (VB) spectra for the pristine and annealed sample (with a −0.5-eV shift applied to the latter).

suggest that the suppression of charge density wave order in 1*T*-VSe_2 could be related to effective electron doping.

To provide further insight into the composition of our samples and to help elucidate the nature of defects, we obtained the crystal stoichiometry from independent laboratory-based XPS measurements (non-monochromatic Al-$k\alpha$ source, $h\nu = 1486.7$ eV) and lattice parameters from powder x-ray diffraction described in Ref. [32]. Shown in Fig. 5 are the results for the *a*- and *c*-axis lattice parameters as a function of the growth temperature together with the variation of crystal stoichiometry for comparison (top axis). First, it can be seen that the stoichiometry (Se/V ratio) of our samples varies from $\mathrm{Se/V} = 1.98 \pm 0.10$ to $\mathrm{Se/V} = 1.94 \pm 0.10$ with increasing growth temperature, which is consistent with the electron-doping hypothesis (either V rich or Se deficient). Considering these two scenarios, it is important first to examine changes in the *c*-axis parameter. Overall we find that it decreases with increasing growth temperature, and therefore it is unlikely that there are significant vanadium interstitials between the layers, which may be expected to produce the opposite effect, i.e., an *increase* in the *c*-axis upon expanding the layer distance [40]. This is supported by our XPS and x-ray absorption spectroscopy data [32], which show no additional features that could be linked to extrinsic V species. Hence, we exclude the V-rich ($V_{1+x}Se_2$) scenario, which would otherwise manifest as V interstitials in the vdW gap [22,25]. Instead, we consider what would be the effects of Se deficiency on the crystal structure. A study of controlled Se loss by annealing in the related compound 1*T*-$TiSe_2$ [41] previously showed a decrease in the *c*-axis related to the Ti-Se bond length, as δ increases in $TiSe_{2-\delta}$ and occurs continuously across the range 350°C–950°C. At the same time, a corresponding increase in the *a*-axis was observed. This trend of the *a*- and *c*-lattice parameters is very similar to what we find for 1*T*-VSe_2 in Fig. 5. Therefore, we suggest that our results can be explained by an overall Se deficiency (VSe_{2-x}) at higher growth temperatures due to increasing Se vacancies (defect B in Fig. 1). The desorption of Se at elevated temperatures is in line with previous reports [18,24] and seems to be of greater significance above 600°C–700°C [42], which is consistent with our observations. As Se becomes volatile and leaves behind a vacancy, the majority is lost from the crystal. However, a small proportion may become trapped in-plane as aggregates/clusters or between layers as interstitials (defects C and E in Fig. 1, respectively). This may explain the additional $\mathrm{Se}^{(-)}$ selenium species seen in XPS [Fig. 4(a)]. It could also be possible that some additional Se is incorporated into the crystals due to the Se-rich environment during the growth process. This would likely occur at higher growth temperatures considering the greater energy cost of disrupting the lattice by introducing an aggregate or interstitial compared to a vacancy.

Finally, to mimic the effects of growing crystals at high temperatures, we also performed an annealing experiment to investigate the effect on the Se-3*d* core levels and valence band. Here, we used a μXPS technique with a focused beam spot of 100 μm in order to precisely measure the same region of the sample before and after annealing. Shown in Fig. 6 are the results, which compare the pristine sample (cleaved in ultrahigh vacuum) with that following heat treatment (annealing to 520°C for ∼40 min). Similarly to Ref. [41], we expect annealing to result in Se loss from the sample, leading to a BE shift as the sample becomes overall electron doped. Indeed, this effect is clearly visible in Fig. 6(a) and the inset shows that the core levels are shifted by approximately 0.5 eV. Although this is much larger than the intrinsic shift in Fig. 4(c), the annealing experiments were performed in ultrahigh vacuum ($< 1 \times 10^{-9}$ mbar), as opposed to the Se-rich atmosphere during crystal growth. Given the high vapor pressure of Se (0.07 atm at 520°C), the greater loss of Se in UHV is expected. As discussed previously, the overall electron doping raises the Fermi level, meaning that the core levels shift to a higher binding energy. This is confirmed by analyzing the valence band spectra in Fig. 6(b), where the

same 0.5 eV shift is applied to the annealed sample spectrum such that the main features of the valence band are overlaid. The up-shifted Fermi level position is indicated by the arrow. These results provide further evidence for the electron-doping scenario, specifically due to an overall Se deficiency (VSe_{2-x}).

In summary, there are likely to be two major types of defects in 1*T*-VSe_2 grown by CVT: Se vacancies and trapped Se aggregates or interstitials. Both will contribute to the defect scattering of carriers in electronic transport and hence decrease the RRR. However, the effective binding energy shift in XPS suggests that the dominant defect type is Se vacancies as the system becomes overall electron doped. This is further supported by the Se deficiency from measurements of the crystal stoichiometry, lattice parameters, and annealing experiments. We suggest that the suppression of the CDW order is caused by a deviation from stoichiometry in the form of electron doping which reduces the T_{CDW}, similarly to 1*T*-$TiSe_2$ [25]. Although the density of defects and the doping level are coincidentally linked, we suggest that the CDW is mainly influenced by doping. In fact, a recent STM investigation of the local density of states in the presence of defects showed the CDW gap in 1*T*-VSe_2 to be extremely robust to disorder [43]. In our results, this is evidenced by the fact that the T_{CDW} approaches a maximum as the crystal stoichiometry nears a 2:1 ratio at the lowest growth temperature concomitant with a saturation of the binding energy shift in XPS (doping level). Instead, the crystal purity (RRR) is expected to continue to increase below $T_g = 550\,^{\circ}$C without any significant gain in T_{CDW}. We note that this is approaching the lower limit of reported growth temperatures for 1*T*-VSe_2 and other TMDs using the iodine CVT technique [23]. By decreasing the temperature further, we anticipate that the growth rate will become increasingly slow until the required growth time is impractical or there is insufficient energy for crystallization to occur.

V. CONCLUSION

From electronic transport measurements, we showed that both the CDW transition temperature, T_{CDW}, and the residual resistance ratio (RRR) decrease for 1*T*-VSe_2 crystals grown at higher temperatures. This is the result of an increased density of defects, which primarily manifests as Se vacancies as a result of Se desorption from the final crystal products at elevated temperatures. Therefore, we suggest that 1*T*-VSe_2 becomes overall Se deficient, which is confirmed by stoichiometry analysis and changes in the unit cell parameters from x-ray diffraction. This deficiency leads to an effective electron doping and a resulting up-shift in the Fermi level, which is evidenced by a rigid shift of Se-3*d* core levels to higher binding energies in XPS measurements. Although the crystal purity is reduced at higher growth temperatures (lower RRR values) due to a higher density of defects, we suggest that the effective electron doping due to overall Se deficiency is mostly responsible for the reduction in T_{CDW}. For samples with $T_g < 630\,^{\circ}$C, we see an increase in the CDW transition temperature above the typically reported value of $T_{CDW} \approx 110$ K. Based on this knowledge, we were able to optimize the chemical vapor transport method in order to produce ultrahigh-purity 1*T*-VSe_2 samples with near-ideal stoichiometry at $T_g = 550\,^{\circ}$C with $T_{CDW} = (112.7 \pm 0.8)$ K and maximum RRR ≈ 49.

Our work highlights the importance of carefully controlling the growth conditions of strongly correlated TMDs whose properties are sensitive to defects and deviation from stoichiometry. In addition, the growth of high-purity TMD materials is imperative both for understanding the bulk behavior of these compounds and for providing a suitable source for exfoliation of monolayers and preparation of van der Waals heterostructures.

ACKNOWLEDGMENTS

We thank the Elettra synchrotron for access to the BEAR beamline (Proposal No. 20180358) and the BEAR staff for assistance during measurements, including S. Nannarone and N. Mahne for helpful discussions. Extensive technical support from P. Jones at the University of Bath is gratefully appreciated. We would like to thank S. Cross and S. Friedemann for insightful discussions and sharing of preliminary data. We thank G. Balakrishnan for sharing unpublished information with regard to Ref. [35]. The authors acknowledge funding and support from the EPSRC Centre for Doctoral Training in Condensed Matter Physics (CDT-CMP), Grant No. EP/L015544/1. Finally, we acknowledge the Bristol NanoESCA Facility (EPSRC Strategic Equipment Grant Nos. EP/K035746/1 and EP/M000605/1).

[1] J. A. Wilson, F. J. Di Salvo, and S. Mahajan, Charge-density waves and superlattices in the metallic layered transition metal dichalcogenides, Adv. Phys. **24**, 117 (1975).

[2] K. Rossnagel, On the origin of charge-density waves in select layered transition-metal dichalcogenides, J. Phys.: Condens. Matter **23**, 213001 (2011).

[3] K. Tsutsumi, X-ray-diffraction study of the periodic lattice distortion associated with a charge-density wave in 1*T*-VSe_2, Phys. Rev. B **26**, 5756 (1982).

[4] D. J. Eaglesham, R. L. Withers, and D. M. Bird, Charge-density wave transitions in 1*T*-VSe_2, J. Phys. C. **19**, 359 (1986).

[5] A. H. Thompson and B. G. Silbernagel, Correlated magnetic and transport properties in the charge-density-wave states of VSe_2, Phys. Rev. B **19**, 3420 (1979).

[6] K. Terashima, T. Sato, H. Komatsu, T. Takahashi, N. Maeda, and K. Hayashi, Charge-density-wave transition of 1*T*-VSe_2 studied by angle-resolved photoemission spectroscopy, Phys. Rev. B **68**, 155108 (2003).

[7] V. N. Strocov, M. Shi, M. Kobayashi, C. Monney, X. Wang, J. Krempasky, T. Schmitt, L. Patthey, H. Berger, and P. Blaha, Three-Dimensional Electron Realm in VSe_2 by Soft-X-Ray Photoelectron Spectroscopy: Origin of Charge-Density Waves, Phys. Rev. Lett. **109**, 086401 (2012).

[8] Á. Pásztor, A. Scarfato, C. Barreteau, E. Giannini, and C. Renner, Dimensional crossover of the charge density wave transition in thin exfoliated VSe_2, 2D Mater. **4**, 041005 (2017).

[9] J. Yang, W. Wang, Y. Liu, H. Du, W. Ning, G. Zheng, C. Jin, Y. Han, N. Wang, Z. Yang, M. Tian, and Y. Zhang, Thickness dependence of the charge-density-wave transition temperature in VSe_2, Appl. Phys. Lett. **105**, 063109 (2014).

[10] Y. Ma, Y. Dai, M. Guo, C. Niu, Y. Zhu, and B. Huang, Evidence of the existence of magnetism in pristine VX_2 monolayers (X = S, Se) and their strain-induced tunable magnetic properties, ACS Nano. **6**, 1695 (2012).

[11] M. Bonilla, S. Kolekar, Y. Ma, H. C. Diaz, V. Kalappattil, R. Das, T. Eggers, H. R. Gutierrez, M. H. Phan, and M. Batzill, Strong room-temperature ferromagnetism in VSe_2 monolayers on van der Waals substrates, Nat. Nanotechnol. **13**, 289 (2018).

[12] Z.-L. Liu, X. Wu, Y. Shao, J. Qi, Y. Cao, L. Huang, C. Liu, J.-O. Wang, Q. Zheng, Z.-L. Zhu, K. Ibrahim, Y.-L. Wang, and H.-J. Gao, Epitaxially grown monolayer VSe_2: An air-stable magnetic two-dimensional material with low work function at edges, Sci. Bull. **63**, 419 (2018).

[13] J. Feng, D. Biswas, A. Rajan, M. D. Watson, F. Mazzola, O. J. Clark, K. Underwood, I. Marković, M. McLaren, A. Hunter, D. M. Burn, L. B. Duffy, S. Barua, G. Balakrishnan, F. Bertran, P. Le Fèvre, T. K. Kim, G. van der Laan, T. Hesjedal, P. Wahl, and P. D. C. King, Electronic structure and enhanced charge-density wave order of monolayer VSe_2, Nano Lett. **18**, 4493 (2018).

[14] P. Chen, W. W. Pai, Y.-H. Chan, V. Madhavan, M. Y. Chou, S.-K. Mo, A.-V Federov, and T.-C. Chiang, Unique Gap Structure and Symmetry of the Charge Density Wave in Single-Layer 1*T*-VSe_2, Phys. Rev. Lett. **121**, 196402 (2018).

[15] H. Wang, X. Huang, J. Lin, J. Cui, Y. Chen, C. Zhu, F. Liu, Q. Zeng, J. Zhou, P. Yu, X. Wang, H. He, S. H. Tsang, W. Gao, K. Suenaga, F. Ma, C. Yang, L. Lu, T. Yu, E. H. T. Teo, G. Liu, and Z. Liu, High-quality monolayer superconductor $NbSe_2$ grown by chemical vapour deposition, Nat. Commun. **8**, 394 (2017).

[16] W. Fu, Y. Chen, J. Lin, X. Wang, Q. Zeng, J. Zhou, L. Zheng, H. Wang, Y. He, H. He, Q. Fu, K. Suenaga, T. Yu, and Z. Liu, Controlled synthesis of atomically thin 1T-TaS_2 for tunable charge density wave phase transitions, Chem. Mater. **28**, 7613 (2016).

[17] Q. Yu, L. A. Jauregui, W. Wu, R. Colby, J. Tian, Z. Su, H. Cao, Z. Liu, D. Pandey, D. Wei, T. F. Chung, P. Peng, N. P. Guisinger, E. A. Stach, J. Bao, S. S. Pei, and Y. P. Chen, Control and characterization of individual grains and grain boundaries in graphene grown by chemical vapour deposition, Nat. Mater. **10**, 443 (2011).

[18] J. P. Peng, J. Q. Guan, H. M. Zhang, C. Li. Song, L. Wang, K. He, Q. K. Xue, and X. C. Ma, Molecular beam epitaxy growth and scanning tunneling microscopy study of $TiSe_2$ ultrathin films, Phys. Rev. B **91**, 121113(R) (2015).

[19] D. Zhang, J. Ha, H. Baek, Y.-H. Chan, F. D. Natterer, A. F. Myers, J. D. Schumacher, W. G. Cullen, A. V. Davydov, Y. Kuk, M. Y. Chou, N. B. Zhitenev, and J. A. Stroscio, Strain engineering a $4a \times \sqrt{3}a$ charge-density-wave phase in transition metal dichalcogenide 1T-VSe_2, Phys. Rev. Mater. **1**, 024005 (2017).

[20] A. Castellanos-Gomez, M. Buscema, R. Molenaar, V. Singh, L. Janssen, H. S. J. van der Zant, and G. A. Steele, Deterministic transfer of two-dimensional materials by all-dry viscoelastic stamping, 2D Mater. **1**, 011002 (2014).

[21] K. Hayashi and M. Nakahira, Stability and the equilibrium selenium vapor pressure of the 1*T*-VSe_2 phase, J. Solid State Chem. **24**, 153 (1978).

[22] F. J. Di Salvo and J. V. Waszczak, Magnetic studies of VSe_2, Phys. Rev. B **23**, 457 (1981).

[23] F. Levy and Y. Froidevaux, Structural and electrical properties of layered transition metal selenides $V_xTi_{1-x}Se_2$ and $Ta_xTi_{1-x}Se_2$, J. Phys. C: Solid. State. Phys. **12**, 473 (1979).

[24] B. Hildebrand, C. Didiot, A. M. Novello, G. Monney, A. Scarfato, A. Ubaldini, H. Berger, D. R. Bowler, C. Renner, and P. Aebi, Doping Nature of Native Defects in 1*T*-$TiSe_2$, Phys. Rev. Lett. **112**, 197001 (2014).

[25] F. J. Di Salvo, D. E. Moncton, and J. V. Waszczak, Electronic properties and superlattice formation in the semimetal $TiSe_2$, Phys. Rev. B **14**, 4321 (1976).

[26] C. S. Yadav and A. K. Rastogi, Electronic transport and specific heat of 1T-VSe_2, Solid State Commun. **150**, 648 (2010).

[27] A. Toriumi and S. Tanaka, Galvanomagnetic properties of 1T-VSe_2, Physica B+C **105**, 141 (1981).

[28] H. Hedayat, C. J. Sayers, D. Bugini, C. Dallera, D. Wolverson, T. Batten, S. Karbassi, S. Friedemann, G. Cerullo, J. van Wezel, S. R. Clark, E. Carpene, and E. Da Como, Excitonic and lattice contributions to the charge density wave in 1*T*-$TiSe_2$ revealed by a phonon bottleneck, Phys. Rev. Res. **1**, 023029 (2019).

[29] H. P. B. Rimmington and A. A. Balchin, The growth by iodine vapour transport techniques and the crystal structures of layer compounds in the series TiS_xSe_{2-x}, TiS_xTe_{2-x}, J. Cryst. Growth. **21**, 171 (1974).

[30] S. Nannarone, F. Borgatti, A. DeLuisa, B. P. Doyle, G. C. Gazzadi, A. Giglia, P. Finetti, N. Mahne, L. Pasquali, M. Pedio, G. Selvaggi, G. Naletto, M. G. Pelizzo, and G. Tondello, The BEAR beamline at Elettra, AIP. Conf. Proc. **705**, 450 (2004).

[31] L. Pasquali, A. De Luisa, and S. Nannarone, The UHV experimental chamber for optical measurements (reflectivity and absorption) and angle resolved photoemission of the BEAR beamline at Elettra, AIP. Conf. Proc. **705**, 1142 (2004).

[32] See Supplemental Material at http://link.aps.org/supplemental/10.1103/PhysRevMaterials.4.025002 for a summary of the 1*T*-VSe_2 sample properties, details of powder x-ray diffraction measurements, methods of determining the CDW phase transition temperature, T_{CDW}, and x-ray spectroscopy (XPS and x-ray absorption spectroscopy) of vanadium and iodine core levels.

[33] C. F. van Bruggen and C. Haas, Magnetic susceptibility and electrical properties of VSe_2 single crystals, Solid State Commun. **20**, 251 (1976).

[34] M. Bayard and M. J. Sienko, Anomalous electrical and magnetic properties of vanadium diselenide, J. Solid State Chem. **19**, 325 (1976).

[35] S. Barua, M. C. Hatnean, M. R. Lees, and G. Balakrishnan, Signatures of the Kondo effect in VSe_2, Sci. Rep. **7**, 10964 (2017).

[36] M. Naito and S. Tanaka, Electrical transport properties in 2*H*-NbS_2, -$NbSe_2$, -TaS_2 and -$TaSe_2$, J. Phys. Soc. Jpn. **51**, 219 (2017).

[37] K. Cho, M. Kończykowski, S. Teknowijoyo, M. A. Tanatar, J. Guss, P. B. Gartin, J. M. Wilde, A. Kreyssig, R. J. McQueeney, A. I. Goldman, V. Mishra, P. J. Hirschfeld, and R. Prozorov, Using controlled disorder to probe the interplay between charge order and superconductivity in $NbSe_2$, Nat. Commun. **9**, 2796 (2018).

[38] M. Shenasa, S. Sainkar, and D. Lichtman, XPS study of some selected selenium compounds, J. Electron. Spec. Relat. Phenom. **40**, 329 (1986).

[39] X. Chia, A. Ambrosi, P. Lazar, Z. Sofer, and M. Pumera, Electrocatalysis of layered Group 5 metallic transition metal dichalcogenides (MX_2, M = V, Nb, and Ta; X = S, Se, and Te), J. Mater. Chem. A **4**, 14241 (2016).

[40] E. Morosan, H. W. Zandbergen, B. S. Dennis, J. W. G. Bos, Y. Onose, T. Klimczuk, A. P. Ramirez, N. P. Ong, and R. J. Cava, Superconductivity in Cu_xTiSe_2, Nat. Phys. **2**, 544 (2006).

[41] S. H. Huang, G. J. Shu,W.-W. Pai, H. L. Liu, and F. C. Chou, Tunable Se vacancy defects and the unconventional charge density wave in 1*T*-$TiSe_{2-\delta}$, Phys. Rev. B **95**, 045310 (2017).

[42] L. N. Zelenina, T. P. Chusova, and A. N. Titov, Thermodynamic properties of titanium selenides with variable composition $TiSe_2$-$TiSe_{1.80}$, Russ. Chem. Bull. **60**, 581 (2011).

[43] W. Jolie, T. Knispel, N. Ehlen, K. Nikonov, C. Busse, A. Grüneis, and T. Michely, Charge density wave phase of VSe_2 revisited, Phys. Rev. B **99**, 115417 (2019).